

Dalton Transactions

Accepted Manuscript

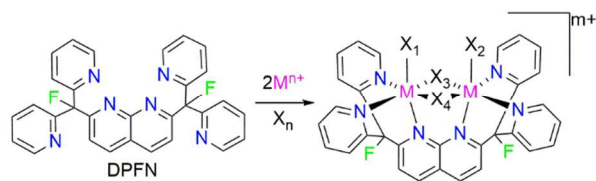


This is an *Accepted Manuscript*, which has been through the Royal Society of Chemistry peer review process and has been accepted for publication.

Accepted Manuscripts are published online shortly after acceptance, before technical editing, formatting and proof reading. Using this free service, authors can make their results available to the community, in citable form, before we publish the edited article. We will replace this *Accepted Manuscript* with the edited and formatted *Advance Article* as soon as it is available.

You can find more information about *Accepted Manuscripts* in the [Information for Authors](#).

Please note that technical editing may introduce minor changes to the text and/or graphics, which may alter content. The journal's standard [Terms & Conditions](#) and the [Ethical guidelines](#) still apply. In no event shall the Royal Society of Chemistry be held responsible for any errors or omissions in this *Accepted Manuscript* or any consequences arising from the use of any information it contains.



A series of “diamond-core” bridged dinuclear first-row transition metal complexes with the dinucleating ligand DPFN are prepared and characterized.

ARTICLE

Dinuclear First-Row Transition Metal Complexes with a Naphthyridine-Based Dinucleating Ligand

Cite this: DOI: 10.1039/x0xx00000x

T.C. Davenport and T. D. Tilley*^a

Received 00th January 2012,

Accepted 00th January 2012

DOI: 10.1039/x0xx00000x

www.rsc.org/

A series of dinuclear and tetranuclear first-row transition metal complexes were synthesized with the dinucleating ligand 2,7-bis(di(2-pyridyl)fluoromethyl)-1,8-naphthyridine (DPFN). The coordination pocket and rigidity of the DPFN ligand enforces pseudo-octahedral geometries about the metal centers that contain chloro, hydroxo, and aqua bridging ligands forming a “diamond” shaped configuration with metal-metal distances varying from 2.7826(5) to 3.2410(11) Å. Each metal center in the dinuclear complexes has an additional open coordination site that accommodates terminal ligands in a *syn* geometry of particular interest in catalyst design. The complexes are characterized by electronic spectroscopy, electrochemistry and potentiometric titration methods.

Introduction

Multinuclear metal centers play an important role in catalytic systems of interest, including metalloenzymes and the active sites of heterogeneous catalysts.^{1–3} In cases involving dinuclear centers, many metalloenzymes are known for which interaction of the two metal centers is thought to play a crucial role in the catalytic function of the enzyme, including hemerythrin,⁴ methane monooxygenase,⁵ ribonucleotide reductase,⁶ urease,⁷ purple acid phosphatase,⁸ catechol oxidase,⁹ and arginase.¹⁰ Indeed, some enzymes containing multinuclear active sites, such as the tetramanganese center in the Oxygen Evolving Complex of Photosystem II, are thought to utilize only two manganese centers in bond-making and bond-breaking events of the catalytic cycle.¹¹ Accordingly, many synthetic water oxidation catalysts with dinuclear metal centers have been developed, such as the ruthenium blue dimer, [(Ru(bpy)₂(OH)₂)]₂(μ-O)[ClO₄]₄.^{12–16} Dinuclear metal complexes are expected to have several advantages over mononuclear complexes including cooperative reactivity of substrates with the neighboring metal centers, lower oxidation or reduction potentials required to store multiple redox equivalents on the complex, enhanced catalysis *via* multielectron processes, and electronic interactions between the metal centers potentially beneficial to catalysis.^{1,17–20}

Interest in the catalytic capabilities of dinuclear metal complexes has led to the study of specially designed dinucleating ligands, for which the structure is tailored to a specific purpose.^{21,22} Such ligands can be designed with several beneficial properties. The ligand can be rigid, enforcing a fixed coordination environment around the metal centers in a manner analogous to that provided by polypeptide frameworks in metalloproteins. Such ligands may also dictate a given metal-metal distance, with controlled electronic interactions between the metal centers.²³ Also, the number and positions of donor atoms can be controlled to achieve a particular coordination geometry, and influence the coordination modes of other ligands.

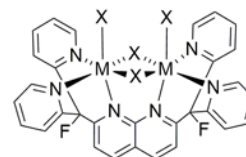
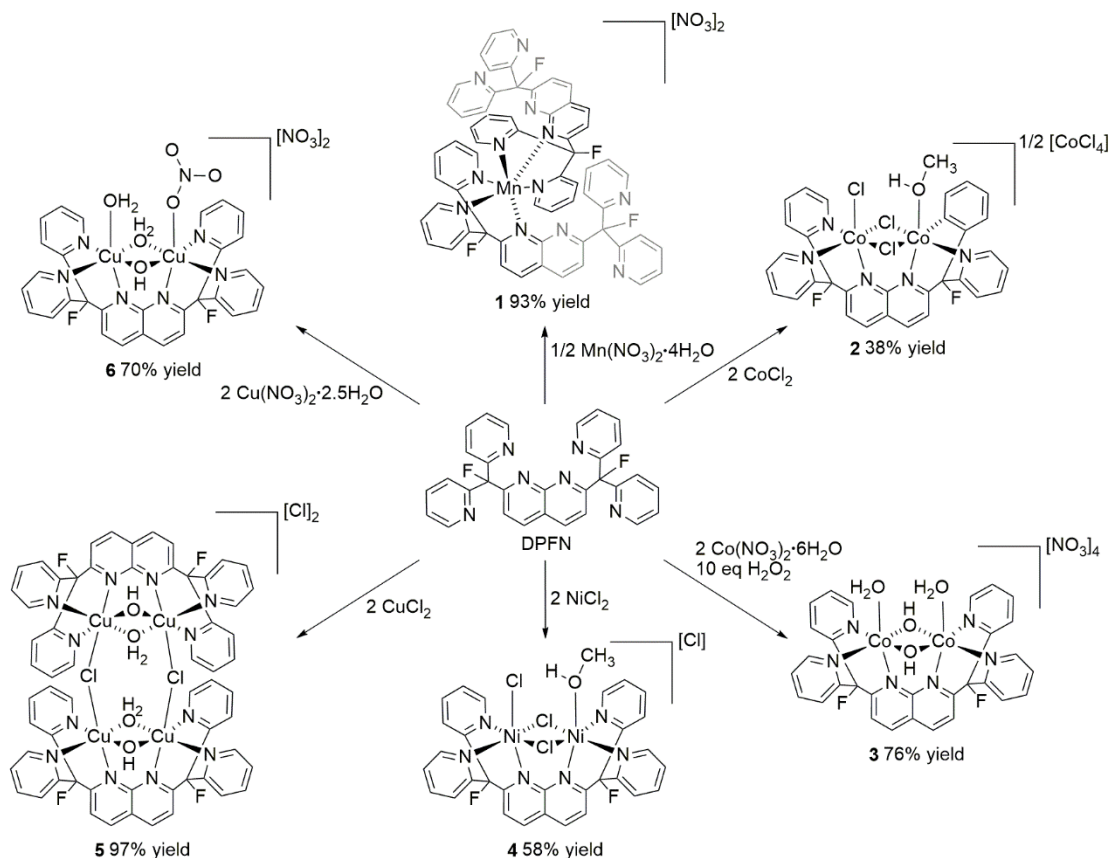


Fig. 1 Coordination geometry of DPFN around two octahedral metal centers. Coordination sites for secondary ligands are represented by the “X” positions.

This report describes the dinucleating properties of a ligand based on the 1,8-naphthyridine core, 2,7-bis(di(2-pyridyl)fluoromethyl)-1,8-naphthyridine (DPFN). The 1,8-naphthyridine core has been described as a “masked carboxylate,” capable of emulating the *syn, syn* bridging mode of the carboxylate group commonly found in biological systems.²⁴ In addition, substitution of the naphthyridine group at the 2 and 7 positions easily affords additional chelating sites at geometric positions favorable for coordination to metal centers bound to the naphthyridyl-N position.^{25–28} In DPFN, the 2 and 7 positions of the naphthyridine core have been substituted with di(2-pyridyl)fluoromethyl groups (Figure 1). This arrangement gives the resulting DPFN ligand six chelating N sites that favorably bind two metal centers, each with 3 N donors coordinated in a *facial* manner. In this arrangement, the metal-metal distance is expected to be in the range of 2.3 to 4.0 Å,²⁸ and, for metal centers preferring octahedral coordination environments, two coordination sites between the two metal centers are suitable for bridging ligands. With two such bridging donor atoms, the dinuclear complex adopts a diamond-shaped configuration. Each metal center has an additional open coordination site that may accommodate terminal ligands in a *syn* geometry. This structural feature is of interest in the design of synthetic molecular water oxidation catalysts,²⁹ as well as other catalysts (e.g., for oxidative dehydrogenation).^{30,31} The following results describe the dinucleating ability of DPFN for

Scheme 1 Synthesis of complexes 1-6.



the first-row transition metals from manganese to copper, with chloro, hydroxo, and aqua bridging ligands that give the diamond-shaped core structure.

Results

Synthesis of DPFN complexes. The DPFN ligand was prepared as described previously.³² Metal DPFN complexes of Mn, Fe, Co, Ni, and Cu were prepared with metal chloride and hydrated metal nitrate starting materials, as shown in Scheme 1. Unlike the later transition elements, manganese did not form a dinuclear metal complex with DPFN in methanol or ethanol, regardless of the number of equivalents of manganese employed. Instead, the complex $[\text{Mn}(\text{DPFN})_2][\text{NO}_3]_2$ (**1**) preferentially formed in these reaction mixtures. By ESI mass spectrometry, it was shown that the $[\text{Mn}(\text{DPFN})_2]^{2+}$ cation was also formed when $\text{Mn}(\text{OTf})_2 \cdot 6\text{H}_2\text{O}$ and $\text{Mn}(\text{ClO}_4)_2 \cdot 6\text{H}_2\text{O}$ were used as starting materials.

Reactions of anhydrous cobalt(II), nickel(II), and copper(II) chloride, or the corresponding hydrated nitrate salts, with DPFN resulted in the formation of dinuclear or tetranuclear metal complexes. For the metal chlorides, two equivalents were added to one equivalent of DPFN in ethanol solution, and the resulting reaction mixture was stirred for 16 h. Evaporation of solvent and

crystallization by vapor diffusion of diethyl ether or tetrahydrofuran into a solution of methanol or ethanol resulted in crystallization of $[\text{Co}_2(\text{DPFN})(\mu\text{-Cl})_2\text{Cl}(\text{MeOH})_2][\text{CoCl}_4]$ (**2**), $[\text{Ni}_2(\text{DPFN})(\mu\text{-Cl})_2\text{Cl}(\text{MeOH})][\text{Cl}]$ (**4**), and $\text{Cu}_2(\text{DPFN})(\mu\text{-Cl})_2\text{Cl}_2$ (**5**), which were isolated and dried at elevated temperatures ($\sim 50^\circ\text{C}$) under dynamic vacuum. In the reaction of CoCl_2 with DPFN in ethanol, green crystals formed on concentration of the mother liquor under vacuum. These crystals could not be redissolved in ethanol, but were recrystallized by vapor diffusion of diethyl ether into a methanol solution to give **2**. This indicates that formation of the CoCl_4^{2-} anion of **2** may be driven by a favorable precipitation from solution. Reactions of the cobalt and copper nitrates, $\text{Co}(\text{NO}_3)_2 \cdot 6\text{H}_2\text{O}$ and $\text{Cu}(\text{NO}_3)_2 \cdot 2.5\text{H}_2\text{O}$, with DPFN in ethanol or methanol led to formation of the hydroxo- or aqua-bridged complexes $[\text{Co}_2(\text{DPFN})(\mu\text{-OH})_2(\text{OH})_2][\text{NO}_3]_4$ (**3**) and $[\text{Cu}_2(\text{DPFN})(\mu\text{-OH})(\mu\text{-OH})_2(\text{OH})_2(\text{NO}_3)][\text{NO}_3]_2$ (**6**). The formation of previously reported **3**,³² unlike the related reactions of the DPFN ligand, results in oxidation of the metal centers. This oxidation occurs spontaneously under laboratory atmosphere; however, the yield of this complex is greatly increased by addition of excess (10 equiv) H_2O_2 to freshly prepared solutions of $\text{Co}(\text{NO}_3)_2 \cdot 6\text{H}_2\text{O}$ and DPFN. If the addition of H_2O_2 is delayed by more than

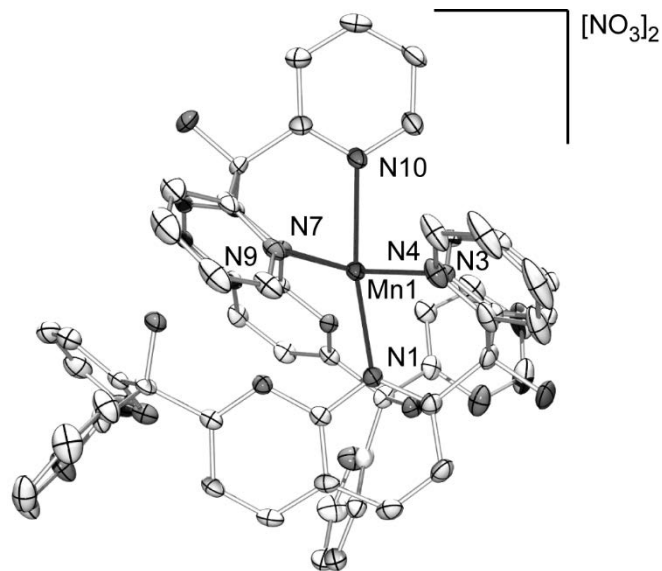


Fig. 2 X-ray crystal structure of **1**. Thermal ellipsoids are shown at 50% probability; hydrogen atoms, solvate molecules, and counterions are omitted for clarity. Selected bond lengths [Å] and angles [°]: Mn1–N1 2.216(2), Mn1–N3 2.234(2), Mn1–N4 2.349(2), Mn1–N7 2.222(2), Mn1–N9 2.249(2), Mn1–N10 2.322(2), N1–Mn1–N10 168.31(7), N4–Mn1–N7 168.73(7), N3–Mn1–N9 165.17(7).

10 min, significant formation of the $[\text{Co}(\text{DPFN})_2]^{2+}$ species (presumably analogous to $[\text{Mn}(\text{DPFN})_2]^{2+}$) was observed by ESI mass spectrometry.

Crystal structures of 1-6. Single crystals of compounds **1-6** were obtained by vapor diffusion of diethyl ether or tetrahydrofuran into methanol or ethanol solutions. The mononuclear manganese compound **1** is shown in Figure 2. The manganese center is bound to two DPFN ligands to give a distorted octahedral geometry, in which each DPFN ligand coordinates in a *facial* manner via two pyridyl and one naphthyridyl nitrogen donors. The distortion from octahedral geometry can be attributed to steric constraints imposed by the accommodation of two DPFN ligands, which results in small N–Mn–N bond angles ($81(3)^\circ$ on average) associated with a given DPFN ligand, and large N–Mn–N bond angles ($107(4)^\circ$ on average) involving separate DPFN ligands.

Crystal structures of the dinuclear and tetranuclear metal complexes **2-6** are shown in Figure 3 and distance and angle measurements are given in Table 1. All of the metal centers in **2-6** are six-coordinate in the solid state with approximate octahedral geometries. For each metal center, three of the coordination sites are occupied by the DPFN ligand in a *facial* coordination manner. The two coordination sites *trans* to the coordinated DPFN pyridyl nitrogens are occupied by the bridging chloro, hydroxo, or aqua ligands, such that the two coordination octahedra for the metal centers share an edge. With the exception of **5**, the coordination site *trans* to the coordinated

Table 1. Selected structural parameters for complexes **2-6**

	2	3	4	5	6
distance (Å) / angle (°)	$\text{Co}_2(\mu\text{-Cl})_2$	$\text{Co}_2(\mu\text{-OH})_2$	$\text{Ni}_2(\mu\text{-Cl})_2$	$[\text{Cu}_2(\mu\text{-Cl})_2]_2$	$\text{Cu}_2(\mu\text{-OH})(\mu\text{-OH}_2)$
M1–M2	3.2382(8)	2.7826(5)	3.2217(8)	3.2410(11)	2.9534(3)
M1–Cl/O1	2.3995(11)	1.8703(16) ^a	2.3504(13)	2.2927(14)	2.0905(12)
M1–Cl/O2	2.3968(12)	1.8787(17)	2.3674(13)		1.9204(11)
M2–Cl/O1	2.4326(11)		2.3672(13)	2.2961(14)	2.0842(11)
M2–Cl/O2	2.3878(11)		2.3877(12)		1.9136(11)
M1–N1	2.250(3)	1.941(2)	2.180(3)	2.609(4)	2.4056(13)
M2–N2	2.346(3)		2.233(4)		2.3767(13)
M1–N3	2.108(3)	1.918(2)	2.057(4)	2.015(4)	2.0069(13)
M1–N4	2.120(3)	1.9306(2)	2.068(4)	2.005(4)	2.0085(13)
M2–N5	2.095(3)		2.063(4)		1.9787(14)
M2–N6	2.126(3)		2.075(4)		2.0210(13)
M1–X (terminal) ^b	2.045(3)	1.908(2)	2.076(3)	2.6421(9)	2.3004(13)
M2–X (terminal) ^c	2.4132(11)		2.3893(13)		2.3747(12)
M1–Cl/O1–M2	84.15(4)	95.85(7)	86.14(4)	89.87(5)	90.05(4)
M1–Cl/O2–M2	85.19(4)		85.30(4)		100.76(5)
equatorial plane angle ^d	26.68(8)	12.14(2)	25.57(7)	36.61(5)	25.64(5)

^aDue to C_2 symmetry, only half of the parameters for **3** and **5** are unique. The atom labels are modified as follows: M2 = M1', Cl/O2 = O1', N3 = N2, N4 = N3. ^bX = (**2**) O1, (**3**) O2, (**4**) O1, (**5**) Cl2, (**6**) O3. ^cX = (**2**) Cl3, (**4**) Cl3, (**6**) O4.

^dDefined as the angle between the least squares planes determined by (M1 N3 N4 Cl/O1 Cl/O2) and (M2 N5 N6 Cl/O1 Cl/O2).

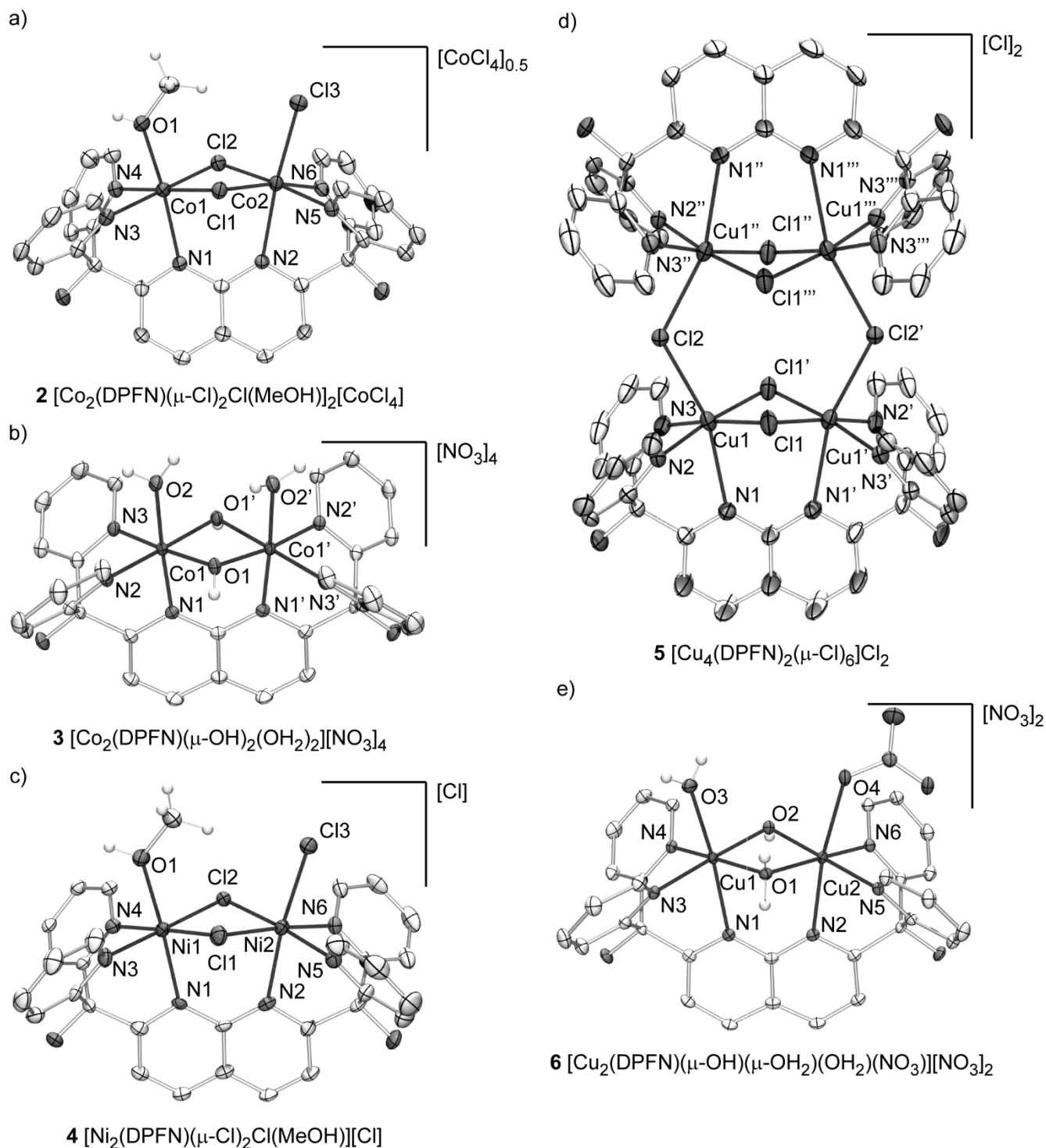


Fig. 3 Crystal structures of complexes **2-6**. Thermal ellipsoids are shown at 50% probability; hydrogen atoms of DPFN, solvate molecules, and counterions are omitted for clarity.

naphthyridine nitrogen is occupied by terminal chloro, aqua, methanol, or nitrate ligands. In the tetranuclear complex **5**, the chloro ligands *trans* to the coordinated naphthyridine nitrogens form a bridge between two facing $\text{Cu}_2(\mu\text{-Cl})_2(\text{DPFN})$ moieties. The $\text{M}_2(\mu\text{-X})_2$ metal-metal distances in **2-6** range from 2.7826(5) to 3.2410(11) Å, and correlate well to the oxidation state of the

metal and the metal-bridging ligand bond lengths. Thus, the higher 3+ oxidation state of cobalt, and thus smaller ionic radius, in **3** compared to the other complexes all containing M(II) centers results in the shortest metal-metal distance of 2.7826(5) Å. Also, the shorter bond lengths to the hydroxo and aqua bridging ligands of 1.917(5) Å and 2.087(4) Å, respectively, in

Table 2. Physical Properties of complexes 1-6

		magnetic moment (μ_B)	d-d transition (nm ($M^{-1}cm^{-1}$))	
1	$[Mn(DPFN)_2]^{2+}$	5.85(16)		
2	$Co_2(\mu-Cl)_2$	4.84(16)	512 (83(5))	485 (88(5))
3	$Co_2(\mu-OH)_2$	diamagnetic	522 (300(10))	362 (sh) ^a
4	$Ni_2(\mu-Cl)_2$	3.04(10)	625 (11.6(4))	
5	$[Cu_2(\mu-Cl)_2]_2$	1.61(5)	702 (180(10))	431 (170(10))
6	$Cu_2(\mu-OH)(\mu-OH_2)$	1.67(5)	599 (52(3))	

^ash = shoulder

the copper complex **6**, results in a metal-metal distance of 2.9534(3) Å while the chloro-bridged copper complex **5**, with an average M-(μ -Cl) bond length of 2.294(2), has a metal-metal distance of 3.2410(11).

For each of the complexes, the M-N naphthyridine bond lengths are longer than the M-N pyridine bond lengths indicating that the N atoms of the naphthyridine are weaker donors than the N atom of pyridine. This likely results from the binding of two Lewis-acid metal ions to the naphthyridine core. Jahn-Teller distortions are most evident in the M-N naphthyridine bond lengths of the d^9 copper complexes **5** (2.609(4) Å) and **6** (av 2.39(2) Å). These bond lengths are significantly longer than the average Cu-N pyridine bond lengths of 2.010(7) (for **5**) and 2.004(18) Å (for **6**). For the d^7 -cobalt centers in complex **2**, the distortion is less pronounced with an average Co-N naphthyridine bond length of 2.21(4) Å and an average Co-N pyridine bond length of 2.066(8) Å.

In general for these complexes, deviation from planarity for the equatorial planes defined by the MN_2X_2 atoms (metal, pyridyl nitrogen atoms and bridging X groups) is small. Root-mean-square deviations for the equatorial MN_2X_2 planes range from 0.030 Å for **4** to 0.061 Å for **2**. In **2**, the largest deviation, 0.106(1) Å, occurs for Co2 which is drawn out of the equatorial MN_2X_2 plane by interaction with the terminal chloro ligand. In contrast, Co1, for which the terminal ligand is methanol, deviates from its MN_2X_2 least-squares plane by only 0.010(1) Å. Similarly, in **4** the largest deviation from the equatorial MN_2X_2 planes is associated with the terminal-chloride-bound Ni2 (0.056(1) Å) while the methanol-bound Ni1 exhibits no significant deviation (0.001 (1) Å). Complex **5** exhibits a relatively large out-of-plane deviation of 0.091(2) Å for Cu1, which is possibly associated with the unique tetranuclear structure, while the other dinuclear structures exhibit relatively small maximum deviations of 0.0595(6) Å for **6**, 0.056(1) Å for **4**, and 0.049(2) for **3**.

Another structural parameter that varies significantly in **2-6** is the angle made between the $M1N_2X_2$ and $M2N_2X_2$ equatorial planes. Ideally, with pure octahedral geometries for the metal centers and an ideal fit inside the pocket of the ligand, the

$M1N_2X_2$ and $M2N_2X_2$ equatorial planes would be coplanar. However, in each complex these planes are angled such that the single-atom bridging ligands are puckered away from the naphthyridine ring of the DPFN ligand. The angle between the equatorial planes varies from 12.14(2)° for **3** to 36.61(5)° for **5**. The variation in this angle is consistent with two main factors: the identity of the bridging ligands, and Jahn-Teller distortion. Because of the short interatomic distance between the nitrogen atoms of the 1,8-naphthyridine fragment (2.298(16) Å), the optimal M-X bond length for an idealized octahedral geometry is ~1.62 Å. Since the M-Cl bonds at 2.36(5) Å are relatively long compared to the M-OH and M-OH₂ bonds, the chloride bridging ligands in **2** and **5** enforce greater angles between the equatorial planes, 26.68(8)° and 36.61(5)°, respectively, than for the hydroxo- or aqua-bridged analogs of the same metal – 12.14(2)° for **3** and 25.64(5)° for **6**. The other factor, Jahn-Teller distortion, results in long M-N(naphthyridine) bonds (*vide supra*), which push the metal centers out of the “pocket” of the ligand, and enforce tilted MN_2X_2 equatorial planes to maintain an octahedral geometry about the metal centers. Thus, the largest angle of 36.61(5)° occurs for the d^9 -copper complex **5** having the largest Jahn-Teller distortion, followed by the moderately Jahn-Teller distorted d^7 -cobalt complex **2** with an angle of 26.68(8)°, and the non-distorted d^8 -nickel complex **4** with an angle of 25.57(7)°. Finally, the smallest angle of 12.14(2)° occurs for the Co(III) complex **3**, consistent with the small ionic radius of the Co(III) ion, which allows the metal centers to better fit into the ligand “pocket.”

Magnetic Measurements. The magnetic moments of complexes **1-6** (Table 2) were measured by the Evans method.³³ With the exception of **3**, the only complex not containing M(II) metal centers, the magnetic moment of each complex is consistent with the spin state expected for high-spin M(II) metal centers. The magnetic moment of the mononuclear d^5 manganese complex **1** is 5.8(2) μ_B , consistent with a high-spin $S = 5/2$ Mn(II) center. The d^7 cobalt complex **2** exhibits a magnetic moment of 4.8(2) μ_B per metal center, a deviation from the spin-only $S = 3/2$ value of 3.87 μ_B typical for high-spin octahedral Co(II) complexes.³⁴ The magnetic moment of the d^8 nickel complex **4**,

$\mu_{\text{eff}} = 3.0(1) \mu_{\text{B}}$ per nickel center, is slightly higher than the spin-only $S = 1$ value ($2.83 \mu_{\text{B}}$), as is usually observed for Ni(II) centers.³⁴ Similarly, for the d^9 copper complexes, the magnetic moments of $1.61(5) \mu_{\text{B}}$ (**5**) and $1.67(5) \mu_{\text{B}}$ (**6**) per copper center are lower than the spin-only value of $1.73 \mu_{\text{B}}$, and also lower than the typically observed magnetic moment for mononuclear Cu(II) centers. However, this behavior is consistent with what has been reported for multinuclear copper complexes and is presumably due to ligand-mediated magnetic exchange between the copper centers.³⁴ In contrast to the M(II) complexes, the Co(III) complex **3** adopts a low-spin, d^6 electronic configuration and is diamagnetic.

Electronic Spectra. Electronic spectra of DPFN and complexes **1-6** were recorded in acetonitrile (DPFN), methanol (**1,2,4,5**), or aqueous (**3,6**) solution. These spectra are shown in Figure 4 and selected absorption peaks are given in Table 2. Each complex exhibits intense electronic transitions in the UV region below ~ 350 nm with high molar absorptivities ($\epsilon > 10,000 \text{ M}^{-1}\text{cm}^{-1}$) composed of one absorption band in the region 308-321 nm, and additional transitions at 255-262 nm and 212-214 nm that are not observed in some complexes. These transitions correspond to those observed in DPFN and are assigned to $\pi-\pi^*$ transitions of the DPFN ligand.

Absorptions corresponding to $d-d$ transitions are observed in each metal complex, with the exception of **1**. As is common for high-spin d^5 centers, the $d-d$ transitions for the d^5 manganese complex **1** are too weak to be observed. The observed bright yellow color of the compound is attributed to broadening of the absorbance peak of the $\pi-\pi^*$ transition at 321 nm, and may arise from unresolved charge transfer bands below 450 nm.

Unlike the other metal complexes, the green crystals of d^7 cobalt complex **2** change color when dissolved in methanol, to give a red solution. This color change can be attributed to reaction of the CoCl_4^{2-} counterion with the water present in solution to form the $\text{Co}(\text{H}_2\text{O})_6^{2+}$ ion. Whereas the CoCl_4^{2-} ion has a complicated set of absorbance peaks in the region 593-693 nm with $\epsilon = 122\text{-}653 \text{ M}^{-1}\text{cm}^{-1}$, the $\text{Co}(\text{H}_2\text{O})_6^{2+}$ ion has only a very weak absorption ($\epsilon = 4.8 \text{ M}^{-1}\text{cm}^{-1}$) at 513 nm which corresponds well with the observed absorption at 512 nm.³⁵

The d^6 cobalt complex **3** has one well-defined $d-d$ transition at 522 nm, as expected for six-coordinate, pseudo-octahedral, low-spin d^6 -cobalt complexes, corresponding to the ${}^1\text{A}_{1g} \rightarrow {}^1\text{T}_{1g}$ transition in pure O_h symmetry. The higher energy ${}^1\text{A}_{1g} \rightarrow {}^1\text{T}_{2g}$ transition occurs in a region partially obscured by the $\pi-\pi^*$ transitions of the DPFN ligand in **3**; however, a shoulder at 362 nm may be assigned to this $d-d$ transition. From the energies of these two transitions, an approximate average crystal field splitting parameter of $\Delta = 21,000 \text{ cm}^{-1}$ can be obtained using the Tanabe-Sugano diagram ($C/B = 4.42$) for d^6 ions. This splitting energy is between the values for $\text{Co}(\text{H}_2\text{O})_6^{3+}$ ($20,760 \text{ cm}^{-1}$) and $\text{Co}(\text{NH}_3)_6^{3+}$ ($22,870 \text{ cm}^{-1}$), which is expected given the mixture of aqua, hydroxo, and pyridine-type ligands in **3**, and suggests that the field strength of the DPFN ligand is similar to that of pyridine.³⁶

The d^8 nickel complex **4** exhibits one weak ($\epsilon = 11.6(4) \text{ M}^{-1}\text{cm}^{-1}$) transition at 625 nm consistent with the intermediate

energy, spin-allowed $d-d$ transition for a six coordinate pseudo-octahedral complex. The other two expected transitions are not observed; however, the tail of the low energy transition absorption band is apparent at 800-900 nm at the low energy limit of the spectrum. The expected high-energy transition is obscured by the $\pi-\pi^*$ transitions of DPFN, but a slight shoulder around 375 nm is evident.

The d^9 copper complexes **5** and **6** are subject to strong Jahn-Teller distortions which are evident in the electronic spectra of these complexes. For the $\text{Cu}_2(\mu\text{-OH})(\mu\text{-OH}_2)$ complex **6**, the Jahn-Teller effect is manifested in the very broad character of the $d-d$ transition with $\lambda_{\text{max}} = 599$ nm. In **5**, the Jahn-Teller effect is large enough to result in two strongly blue-shifted, distinct absorptions corresponding to a low energy $d_{z^2} \rightarrow d_{xy}$ transition at 702 nm and a high energy $d_{x^2-y^2}, d_{xz}, d_{yz} \rightarrow d_{xy}$ transition at 431 nm. The absorption peak at 431 nm is unusually high in energy for a $d-d$ transition in a Cu(II) complex but is too weak ($\epsilon = 170(10) \text{ M}^{-1}\text{cm}^{-1}$) to correspond to a charge transfer band.

Electrochemical Experiments. Cyclic voltammetry traces of DPFN and compounds **1-6** were recorded in 0.1 M $n\text{-Bu}_4\text{NPF}_6$ DMF with a glassy carbon electrode using a Ag/AgNO₃ reference electrode in acetonitrile. The CV traces shown in Figure 5 are referenced to Fc/Fc⁺ (0.076 V vs. Ag/AgNO₃ in acetonitrile). Due to insolubility of **3** in 0.1 M $n\text{-Bu}_4\text{NPF}_6$ DMF solution, two equivalents of 1 M KOH aqueous solution were added to solubilize the complex.

The cyclic voltammetry of DPFN in Figure 5a shows that the compound is anodically stable in DMF and cathodically stable to -1.8 V after which DPFN is reduced at a peak cathodic current at -1993 mV, assigned to reduction of the naphthyridine moiety. An additional, significant reduction event occurs at -2650 mV assigned to reduction of the pendant pyridine rings (for pyridine $E_{1/2} = -2.66$ V vs. SCE in 0.1 M Et₄Ni DMF³⁷). Reoxidation of DPFN is not observed except for a small anodic current at -788 mV indicating decomposition of the DPFN upon reduction. In **1-6**, oxidation and reduction events are observed between -1.8 and 1.2 V. In the mononuclear manganese complex **1**, reduction of the complex is observed in two events at -1656 mV and -1759 mV. These reduction events may either correspond to reduction of the DPFN ligands (shifted to more cathodic potentials compared to free DPFN due to complexation to the metal center) or to metal-based reductions of Mn^{II} to Mn^{I} , followed by reduction from Mn^{I} to Mn^{0} . No oxidation of Mn^{II} to Mn^{III} is observed below 1.2 V.

For the series of chloride-bridged complexes **2, 4, and 5**, analogous oxidation and reduction events are observed. For the dinickel complex **4**, one broad reduction event is observed with a cathodic current peak at -1449 mV, associated with a corresponding reoxidation at -1302 mV, and appears to contain multiple overlapping reduction events. This reduction may correspond to reduction of the DPFN ligand or metal-based reduction to $\text{Ni}^{\text{I}}\text{Ni}^{\text{I}}$. Oxidation of **4** is observed as a broad oxidation step with an anodic peak at 599 mV, associated with re-reduction at 349 mV. This oxidation wave appears to contain two distinct oxidation events, and so the oxidized species is assigned to the $\text{Ni}^{\text{III}}\text{Ni}^{\text{III}}$ state. Reduction of the tetranuclear

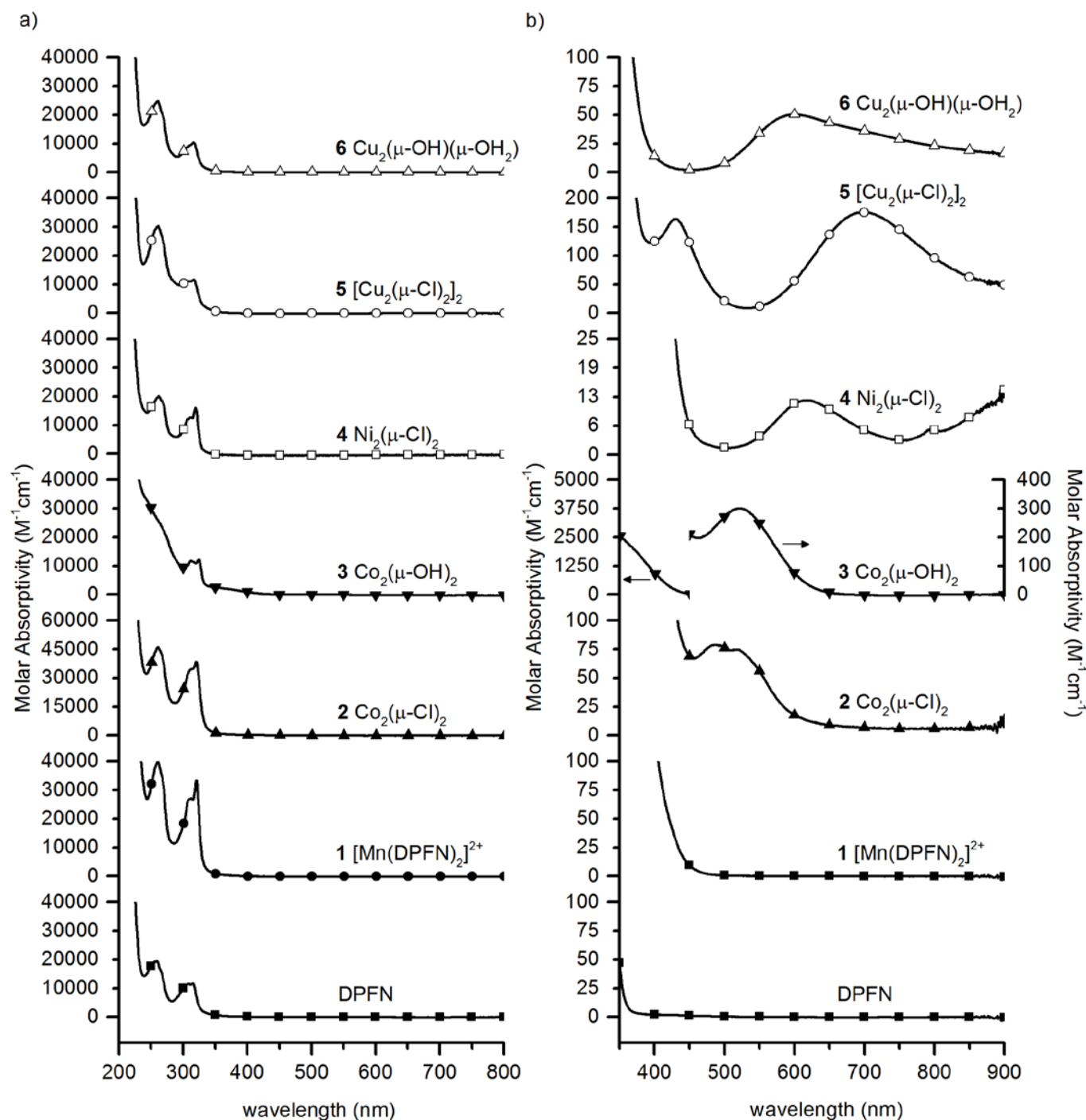


Fig. 4 Electronic spectra of DPFN (■), 1 (●), 2, (▲), 3 (▼), 4 (□), 5 (○), and 6 (△). a) Spectral region from 200–800 nm displaying high intensity features with molar absorptivity up to 60,000 M⁻¹ cm⁻¹. b) Spectral region from 350–900 nm displaying low intensity features with molar absorptivity less than 5000 M⁻¹ cm⁻¹.

copper complex 5 occurs in two reduction events at -235 mV and at -592 mV. Tentatively these reductions are assigned to the intermediate Cu^ICu^ICu^{II}Cu^{II} species followed by the Cu^ICu^ICu^ICu^I species, however, it is also reasonable that the tetranuclear structure dissociates into dinuclear units when dissolved in DMF and the reduction steps may represent Cu^ICu^{II}

and Cu^ICu^I species. Due to the lack of an associated reoxidation wave for the reduction at -592 mV, the complex likely decomposes. Re-oxidation of the metal centers to Cu^{II} species then occurs at -15 mV. Oxidation of the complex occurs in two unresolved steps with an anodic peak at 645 mV and a cathodic peak at 365 mV. Based on the size of the peak, the presence of

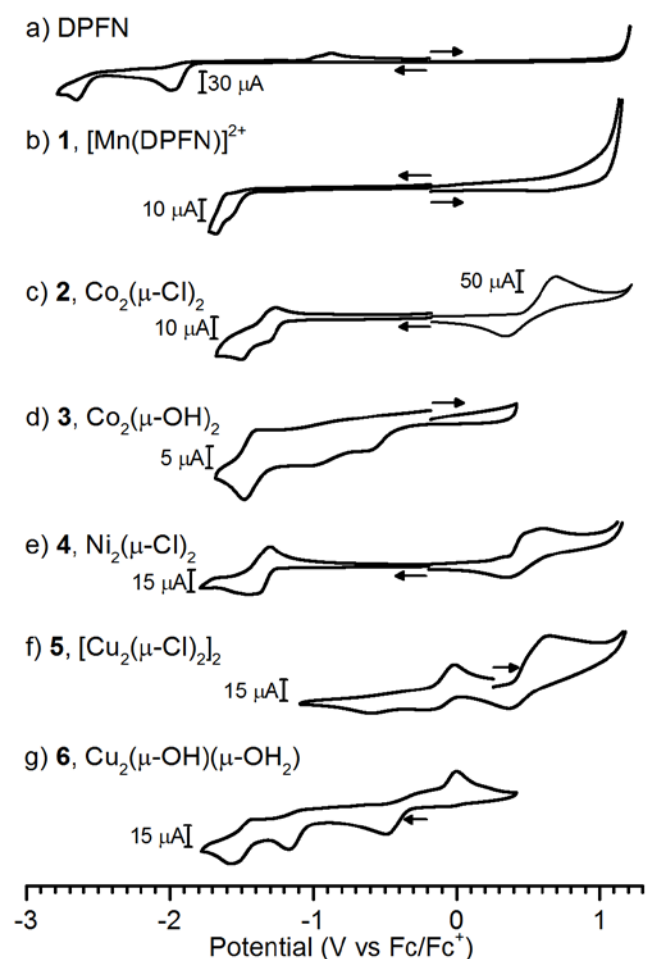


Fig. 5 Cyclic voltammograms of 2 mM DMF solutions of a) DPFN, b) **1**, c) **2**, d) **3**, e) **4**, f) **5**, g) **6**. Voltammograms are shown on a common potential scale referenced to Fc/Fc⁺. The direction of the initial scanning potential for each experiment is indicated by an arrow. For DPFN and **1**, two separate cyclic voltammograms for anodic and cathodic potentials are given. For **2**, anodic potentials are scaled to 50 μ A while cathodic potentials are scaled to 10 μ A.

two oxidation steps and the likelihood that the reduction steps either occur as two electron reductions or the complex dissociates to dinuclear units in DMF solution, the oxidized species is tentatively assigned to oxidation of all the copper centers to Cu^{III}. In the cobalt complex **2**, reduction is observed in two steps with cathodic current peaks at -1298 mV and -1500 mV. As with complex **4**, the reduction might be attributable to reduction of the DPFN ligand or to reduction of the metal centers to Co^ICo^I. Anodic reoxidation associated with the first reduction step is observed at -1263 mV. Scanning to anodic potentials with **3** results in one high current redox event with $E_{1/2} = 518$ mV attributed to oxidation of the CoCl₄²⁻ anion. Oxidation of the Co^{II}Co^{II} cation is not observed but may be obscured by the oxidation of CoCl₄²⁻.

The hydroxo- and aqua-bridged complexes **3** and **6** show significantly different electrochemical properties as compared to the related chloride-bridged complexes. The hydroxide-bridged cobalt complex **3** is strongly stabilized in the Co^{III}Co^{III} oxidation state, with respect to the chloride-bridged cobalt complex **2**. The

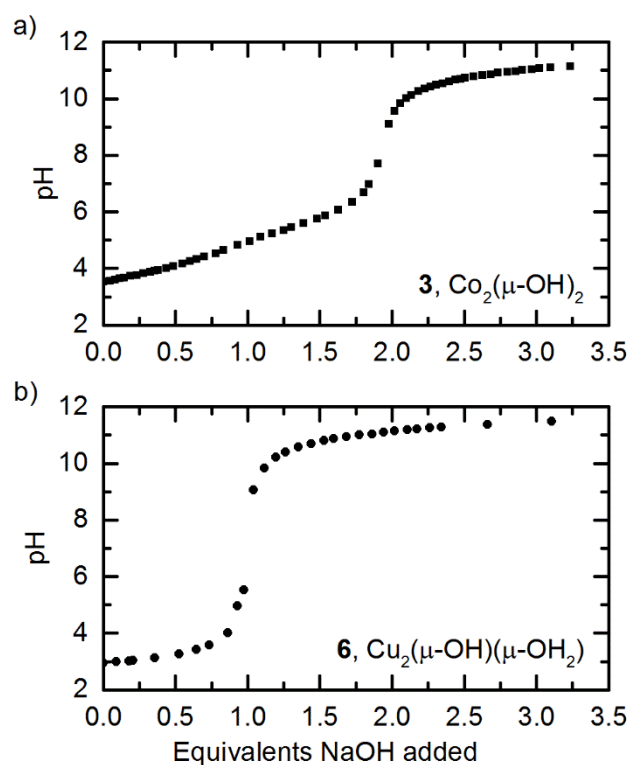


Fig. 6 Potentiometric titration curves of **3** (■), and **6** (●). Base was added as aliquots of a 0.1 M NaOH solution.

Co^{III}Co^{III} state is not observed for **2**, although due to the obscuring presence of CoCl₄²⁻ its formation could occur above a potential as low as 524 mV. The stabilization of the Co^{III}Co^{III} oxidation state in **3** relative to **2** is attributed to strong stabilizing interactions between the electron lone pairs of the μ -hydroxo ligands with the empty orbitals of the Co^{III} ions. This stabilizing interaction is reflected in the large number of known dinuclear Co^{III} bis- and tris- μ -hydroxo complexes.³⁸ Reduction of the Co^{III}Co^{III} state of **3** occurs in two separate steps to form the Co^{III}Co^{II} state at -619 mV and the Co^{II}Co^{II} state at -985 mV. These reduction steps are completely irreversible, probably due to major structural changes that occur on reduction to the labile Co(II) oxidation state. Further reduction of the complex with a ligand-based reduction or to a Co^ICo^I species occurs with cathodic current peaks at -1481 mV, with re-oxidation at -1375 mV. Oxidation of **3** to Co^{IV}Co^{III} or Co^{IV}Co^{IV} species is not observed to 1.2 V.

The hydroxo- and aqua-bridged copper complex **6** exhibits significant stabilization of the Cu^{II}Cu^{II} state compared to the Cu^{II}Cu^I state in the chloride-bridged complex **5**. While oxidation of **5** is observed at 738 mV, tentatively attributed to oxidation to Cu^{III}, oxidation of **6** is not observed up to 1.2 V. Also, while the reduction of **5** to a Cu^I-only species occurs in two steps at -223 mV and -580 mV, the reduction of **6** to Cu^ICu^I occurs in two steps with cathodic current peaks at -491 mV and -1170 mV indicating a much more stable Cu^{II}Cu^I mixed-valence state, as well as a stabilized Cu^{II}Cu^{II} state (with respect to **5**). Re-oxidation to Cu^{II}Cu^{II} occurs with an anodic current peak at -3 mV. In

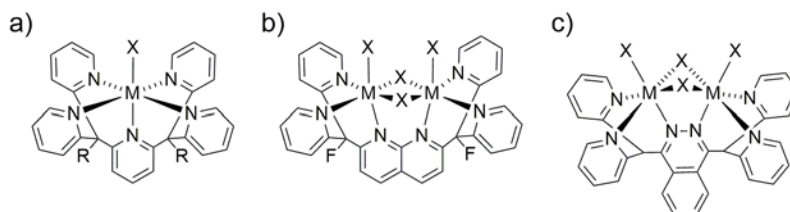


Fig. 7 Comparison of the coordination modes of a) Py5, b) DPFN, and c) bdptz.

addition to reduction to the $\text{Cu}^{\text{I}}\text{Cu}^{\text{I}}$ state for **5**, further ligand-based reduction or metal-based reduction to Cu^0 occurs with a cathodic current peak at -1573 mV with partial re-oxidation ($i_{\text{pa}}/i_{\text{pc}} = 0.2$) occurring at an anodic current peak at -1406 mV.

Acid Dissociation Constants of 3 and 6. The hydroxo- and aqua-bridged complexes **3** and **6** contain terminal or bridging aqua ligands that should exhibit acidic properties. The acid dissociation constants for these complexes were determined by potentiometric titration of aqueous solutions of **3** or **6** using a 0.1 M NaOH solution (Figure 6). For the cobalt complex **3**, two terminal aqua ligands could be deprotonated, with acid dissociation constants measured from the half-equivalence points as $\text{pK}_{\text{a}1} = 4.1(1)$ and $\text{pK}_{\text{a}2} = 5.8(1)$. In the copper complex **6**, the bridging aqua ligand is deprotonated with an acid dissociation constant of $\text{pK}_{\text{a}} = 3.3(1)$.

Discussion

This work has produced a range of first-row transition metal dinuclear and tetranuclear complexes formed by the naphthyridine-based dinucleating ligand DPFN. Comparisons of DPFN can be made with the well-known pentadentate ligand Py5, and the analogous phthalazine-based dinucleating ligand bdptz, which have similarly been used to form a series of first-row transition metal complexes (Figure 7) and is representative of several dinucleating ligands with *facial* tridentate N atom binding sites that may also be pyrazolyl- or pyridazine-based.^{39–43} DPFN may be regarded as the dinucleating analog of Py5. Like Py5, stable complexes with DPFN tend to contain metals in the $2+$ oxidation state having a high-spin electronic configuration. A comparison of chloride complexes of the DPFN and Py5 ($\text{R} = \text{OMe}$) ligands shows that $\text{M}-\text{N}(\text{pyridyl})$ distances are slightly shorter for the DPFN complexes, by an average of $0.07(6)$ Å. In addition, the $\text{M}-\text{N}(\text{naphthyridine})$ distances in DPFN complexes are on average $0.15(5)$ Å longer than the $\text{M}-\text{N}$ bond distance associated with the axial pyridine of Py5 complexes. This likely reflects the weaker donating ability of the naphthyridine N atoms when coordinated to two metal ions but may also reflect the operation of strain, induced by the placement of two metal centers in the binding pocket of DPFN. Comparison of the electrochemical properties of DPFN and Py5 complexes shows that DPFN complexes tend to exhibit more irreversible oxidation or reduction events, while Py5 complexes often display reversible redox events. This may be due to the greater

flexibility of the ligand pocket of DPFN versus Py5, allowing for significant structural changes during redox events. Also, this may be indicative of greater instability of DPFN complexes due to tridentate binding to each metal center instead of pentadentate binding as exhibited by Py5.

The electrochemical properties of the nickel chloride complexes of DPFN and Py5 are the most directly comparable due to the presence of multiple, analogous redox events. In the $[(\text{Py}5)\text{NiCl}][\text{Cl}]$ complex, oxidation to Ni^{III} occurs at $E_{1/2} = 0.39$ V (*vs.* Fc/Fc^+) while reduction to Ni^{I} occurs as $E_{1/2} = -1.91$ V. In the dinuclear complex **4**, oxidation to the $\text{Ni}^{\text{III}}\text{Ni}^{\text{III}}$ state is observed at $E_{1/2} = 0.47$ V and reduction to the $\text{Ni}^{\text{I}}\text{Ni}^{\text{I}}$ state occurs at $E_{1/2} = -1.38$ V (if the reduction is solely metal-based). The shift of the oxidation and reduction events to more positive potentials in **4** is likely due to the presence of three chloride ligands and only three nitrogen donors for each metal center instead of a single chloride and five nitrogen donors in $[(\text{Py}5)\text{NiCl}][\text{Cl}]$. However, at only slightly more positive oxidative potentials, **4** is oxidized by two rather than one electron, demonstrating the ability of dinuclear DPFN complexes to store multiple redox equivalents at a lower required potential.

Comparisons can also be made to the similar, dinucleating bdptz ligand (Figure 7c).^{40,41} The ligand bdptz forms related chloride- and hydroxide-bridged complexes, providing useful comparison to the chloride- and hydroxide-bridged DPFN complexes. Due to the coordination geometry of the phthalazine nitrogen atoms, the range of $\text{M}-\text{M}$ distances supported in complexes with bdptz have a greater range of values ($3.754 - 3.121$ Å) compared to complexes of DPFN ($2.7826(5) - 3.2410(11)$ Å). This ability to support long metal-metal distances may explain why bdptz easily forms chloro-bridged dimanganese(II) complexes with an $\text{M}-\text{M}$ distance of $3.549(2)$ Å, while DPFN appears to be more resistant toward formation of complexes with higher ionic radii.

Conclusions

This work illustrates the dinucleating ability of the naphthyridine-based dinucleating ligand DPFN. Dinuclear and tetranuclear metal complexes were formed with late first-row transition metals in which the two metal centers are held at separations of $2.7826(5) - 3.2410(11)$ Å. The structural properties of DPFN are conducive to formation of pseudo-

octahedral metal centers with two one-atom bridging ligands to give “diamond-shaped” dinuclear complexes.

Experimental

General Considerations. Spectroscopic grade solvents were purchased from Aldrich and distilled water was employed. Deuterated solvents were purchased from Cambridge Isotope Laboratories and used as received. The ligand DPFN was prepared as described previously.³² NMR spectra were recorded on a Bruker AV-600 spectrometer at 20 °C. ¹H NMR spectra were referenced to residual protio solvent peaks (δ 4.80 for *d*₂-water, δ 4.78 for *d*₄-methanol). Solution magnetic susceptibilities were determined by the Evans' method.³³ Solution UV-Vis spectra were collected using a Cary 300 Bio spectrophotometer with a 1-cm quartz cell at 1 nm resolution. Infrared spectra were recorded on powders with a Thermo Scientific Nicolet iS10 using the Smart iTR ATR sampling accessory. Potentiometric titrations were performed using a Thermo Fisher Orion 3-Star pH meter with a Ag/AgCl combination pH electrode. Measurement of acid dissociation constants were not corrected for ionic strength. Elemental analyses were carried out by the College of Chemistry Microanalytical Laboratory at the University of California, Berkeley.

Electrochemical Measurements. Electrochemical experiments were recorded with a BASi Epsilon potentiostat using a 3 mm diameter glassy carbon working electrode, a Pt wire counter electrode and a Ag/AgNO₃ reference electrode (0.1 M [¹⁸Bu₄N][PF₆], 1 mM AgNO₃ in ACN, 0.076 V vs. Fc/Fc⁺). The glassy carbon working electrode was polished between runs with 0.05 μ m alumina slurry, rinsed with water and dried. Cyclic voltammograms were recorded in 0.1 M DMF [¹⁸Bu₄N][PF₆] solutions. Solutions were purged with nitrogen before analysis.

Synthesis of [Mn(DPFN)₂][NO₃]₂·5CH₃OH (1). DPFN (0.2 g, 0.4 mmol) was dissolved in 25 mL of MeOH and then Mn(NO₃)₂·4H₂O (0.05 g, 0.2 mmol) was added. The resulting yellow solution was stirred for 16 h. The volume of the solution was reduced to ~5 mL and the product was crystallized from solution by vapor diffusion of THF to afford yellow X-ray quality crystals (0.25 g, 0.18 mmol, 93%). **Magnetic Moment** (Evans³): $\mu_{\text{eff}} = 5.9(2) \mu_{\text{B}}$. **UV-Vis** (MeOH, λ [nm] (ϵ [$\text{M}^{-1}\cdot\text{cm}^{-1}\cdot 10^{-3}$])): 260 (40(3)), 321 (33(2)), 312 (27(2)). **IR** (ATR, $\tilde{\nu}$ [cm^{-1}]): 1598(m), 1504(w), 1469(m), 1434(m), 1338(s), 1301(w), 1214(w), 1136(m), 1101(w), 1084(w), 1055(w), 1015(m), 995(w), 933(w), 901(w), 859(m), 830(w), 775(s), 749(m), 714(w), 700(w), 689(s), 641(w), 617(w), 593(w), 559(w), 543(w). **EA** Anal. Calcd (%) for C₆₅H₆₀F₄MnN₁₄O₁₁ (1344.21 g/mol): C, 58.08; H, 4.50; N, 14.59. Found: C, 58.07; H, 4.12; N, 14.97.

Synthesis of [Co₂(μ -Cl)₂Cl(CH₃OH)(DPFN)₂][CoCl₄]·8H₂O (2). Under a flow of nitrogen, DPFN (0.1 g, 0.2 mmol) was dissolved with heating in 75 mL of EtOH and then a solution of anhydrous CoCl₂ (0.05 g, 0.4 mmol) in 10 mL of EtOH was added. The resulting pale orange solution was stirred for 16 h and slowly turned brown in color. The volume of the solution was reduced to ~5 mL, and this solution was allowed to stand at room

temperature for 10 min, after which green crystals of the product formed. The product was recrystallized by vapor diffusion of Et₂O into a MeOH solution to form green X-ray quality crystals (0.06 g, 0.03 mmol, 38%). **Magnetic Moment** (Evans³): $\mu_{\text{eff}} = 11.1(5) \mu_{\text{B}}$. **UV-Vis** (MeOH, λ [nm] (ϵ [$\text{M}^{-1}\cdot\text{cm}^{-1}\cdot 10^{-3}$])): 212 (160(10)), 261 (47(3)), 320 (38(2)), 485 (0.088(5)), 512 (0.083(5)). **IR** (ATR, $\tilde{\nu}$ [cm^{-1}]): 1618(w), 1600(m), 1537(w), 1511(w), 1472(m), 1438(m), 1391(w), 1296(w), 1195(w), 1160(w), 1486(w), 1104(w), 1083(m), 1060(w), 1024(m), 929(w), 856(m), 808(w), 774(s), 713(w), 702(w), 687(m), 642(w), 614(w), 577(w). **EA** Anal. Calcd (%) for C₆₂H₆₄Cl₁₀Co₅F₄N₁₂O₁₀ (1862.45 g/mol): C, 39.76; H, 3.20; N, 9.02. Found: C, 39.98; H, 3.46; N, 9.02.

Synthesis of [Ni₂(μ -Cl)₂Cl(CH₃OH)(DPFN)₂][Cl]·4H₂O (4). Under a flow of nitrogen, DPFN (0.1 g, 0.2 mmol) was dissolved with heating in 75 mL of EtOH and then a solution of anhydrous NiCl₂ (0.05 g, 0.4 mmol) in 10 mL of EtOH was added. The resulting green solution was stirred for 16 h. The solvent was removed by rotovap to give the product as a green precipitate. The product was crystallized by vapor diffusion of Et₂O into a MeOH solution to form green X-ray quality crystals (0.10 g, 0.12 mmol, 58%). **Magnetic Moment** (Evans³): $\mu_{\text{eff}} = 4.3(2) \mu_{\text{B}}$. **UV-Vis** (MeOH, λ [nm] (ϵ [$\text{M}^{-1}\cdot\text{cm}^{-1}\cdot 10^{-3}$])): 262 (20.0(8)), 313 (14.1(5)), 320 (16.7(6)), 625 (0.0116(4)). **IR** (ATR, $\tilde{\nu}$ [cm^{-1}]): 1602(m), 1578(w), 1541(w), 1512(w), 1471(m), 1441(m), 1395(w), 1296(w), 1239(w), 1196(w), 1161(w), 1142(w), 1086(m), 1061(w), 1026(m), 931(w), 853(m), 772(s), 714(w), 702(w), 686(s), 643(w), 615(w), 576(w), 551(w). **EA** Anal. Calcd (%) for C₃₁H₃₂Cl₄F₂N₆Ni₂O₅ (865.86 g/mol): C, 42.88; H, 3.46; N, 9.84. Found: C, 43.00; H, 3.73; N, 9.71.

Synthesis of [Cu₄(μ -Cl)₆(DPFN)₂][Cl]₂·6H₂O (5). Under a flow of nitrogen, DPFN (0.1 g, 0.2 mmol) was dissolved with heating in 75 mL of EtOH, and to this solution was added a solution of anhydrous CuCl₂ (0.05 g, 0.4 mmol) in 10 mL of EtOH. The resulting bright green solution was stirred for 16 h. The volume of the solution was reduced to ~5 mL, the solution was filtered, and the product was crystallized by vapor diffusion of Et₂O into the EtOH solution to form green X-ray quality crystals (0.16 g, 0.19 mmol, 97%). **Magnetic Moment** (Evans³): $\mu_{\text{eff}} = 2.27(7) \mu_{\text{B}}$. **UV-Vis** (MeOH, λ [nm] (ϵ [$\text{M}^{-1}\cdot\text{cm}^{-1}\cdot 10^{-3}$])): 212 (150(11)), 261 (60(4)), 305 (23(2)), 310 (23(2)), 316 (23(2)), 431 (0.17(1)), 702 (0.18(1)). **IR** (ATR, $\tilde{\nu}$ [cm^{-1}]): 1603(m), 1578(w), 1544(w), 1502(w), 1471(m), 1436(m), 1296(w), 1246(w), 1196(w), 1162(w), 1140(w), 1083(m), 1064(w), 1026(m), 862(m), 811(w), 778(s), 712(w), 699(w), 686(m), 650(w), 618(w), 570(w). **EA** Anal. Calcd (%) for C₆₀H₅₂Cl₈Cu₄F₄N₁₂O₆ (1650.94 g/mol): C, 43.74; H, 3.00; N, 10.13. Found: C, 43.65; H, 3.17; N, 10.18.

Synthesis of [Cu₂(μ -OH)₂(NO₃)(OH₂)(DPFN)₂]-2H₂O (6). DPFN (0.2 g, 0.4 mmol) was dissolved with heating in 20 mL of MeOH to which was added a solution of Cu(NO₃)₂·2.5H₂O (0.19 g, 0.8 mmol) in 10 mL of MeOH and 2 mL of H₂O. The resulting blue solution was stirred for 30 min. The solvent was removed by rotovap to give the product as a blue precipitate. The product

Table 3. Experimental details for the X-ray crystal structures of **1**, **2**, **4**, **5**, **6**

	1	2	4	5	6
Chemical formula	C _{66.5} H ₅₄ F ₄ MnN ₁₄ O ₈	C _{33.875} H ₃₄ Cl ₅ Co _{2.5} F ₂ N ₆ O _{3.125}	C _{34.25} H ₃₇ Cl ₄ F ₂ N ₆ Ni ₂ O _{4.25}	C ₇₀ H ₆₄ Cl ₈ Cu ₄ F ₄ N ₁₂ O ₄	C ₃₀ H ₂₉ Cu ₂ F ₂ N ₉ O ₁₄
Formula Mass	1308.17	937.75	897.89	1751.15	904.7
Crystal system	Monoclinic	Triclinic	Triclinic	Orthorhombic	Monoclinic
<i>a</i> /Å	13.4808(5)	13.6956(16)	11.8504(5)	15.1594(6)	21.1143(19)
<i>b</i> /Å	25.9908(10)	15.6624(18)	13.3500(6)	21.5153(8)	14.7530(13)
<i>c</i> /Å	17.5035(7)	21.613(3)	23.8878(10)	43.7045(17)	23.299(2)
<i>α</i> /°	90	82.380(1)	97.747(2)	90	90
<i>β</i> /°	104.029(2)	73.241(1)	93.565(2)	90	106.1750(10)
<i>γ</i> /°	90	64.529(1)	102.721(2)	90	90
Unit cell volume/Å ³	5949.9(4)	4007.5(8)	3636.2(3)	14254.6(10)	6970.2(11)
Temperature/K	100(2)	100(2)	100(2)	100(2)	100(2)
Space group	<i>P</i> 2 ₁ / <i>c</i>	<i>P</i> $\bar{1}$	<i>P</i> $\bar{1}$	<i>F</i> ddd	<i>C</i> 2/ <i>c</i>
No. of formula units per unit cell, <i>Z</i>	4	4	4	8	8
No. of independent reflections	10866	14648	13562	3262	6390
<i>R</i> _{int}	0.0536	0.0446	0.0399	0.0429	0.0205
Final <i>R</i> _i values (<i>I</i> > 2σ(<i>I</i>))	0.0466	0.0502	0.0598	0.0488	0.0206
Final <i>wR</i> (<i>F</i> ²) values (<i>I</i> > 2σ(<i>I</i>))	0.1163	0.1378	0.1405	0.1318	0.0549
Final <i>R</i> _i values (all data)	0.0661	0.0692	0.0927	0.0754	0.0222
Final <i>wR</i> (<i>F</i> ²) values (all data)	0.1248	0.1529	0.1515	0.1526	0.0558
Goodness of fit on <i>F</i> ²	1.116	1.057	1.097	1.066	1.053

was dissolved in ~3 mL of hot water and crystallized by slow evaporation to give blue X-ray quality crystals (0.25 g, 0.28 mmol, 70%). **Magnetic Moment** (Evans⁷): $\mu_{\text{eff}} = 2.38(8) \mu_{\text{B}}$. **UV-Vis** (water, λ [nm] (ϵ [$\text{M}^{-1}\cdot\text{cm}^{-1}\cdot 10^{-3}$])): 260 (25(1)), 316 (10.4(5)), 599 (0.052(3)). **IR** (ATR, $\tilde{\nu}$ [cm^{-1}]): 1606(m), 1578(w), 1474(w), 1444(w), 1401(s), 1321(s), 1299(s), 1194(w), 1163(w), 1132(w), 1086(m), 1030(m), 1002(w), 930(w), 868(m), 827(w), 811(w), 775(s), 713(w), 699(w), 688(m), 655(w), 620(w), 572(w), 557(w), 539(w). **EA Anal.** Calcd (%) for C₃₀H₂₉Cu₂F₂N₉O₁₄ (904.70 g/mol): C, 39.94; H, 3.19; N, 13.81. Found: C, 39.83; H, 3.23; N, 13.93.

Crystallographic Analyses. X-ray diffraction data were collected for compounds **1**, **2** and **4–6** using Bruker AXS three-circle diffractometers coupled to a CCD detector with graphite or QUAZAR multilayer mirror monochromated Mo K α ($\lambda = 0.71073 \text{ \AA}$) radiation cooled under a stream of N₂ to 100 K. Raw data were integrated and corrected for Lorentz and polarization effects using Bruker APEX2 v. 2009.1. Absorption corrections were applied using SADABS. The structures were solved by

direct methods using SHELXS and refined against *F*² on all data by full-matrix least squares with SHELXL-97. Refinement details for each compound are detailed below:

[Mn(DPN)₂][NO₃]₂·0.5CH₃OH·1.5THF (**1**). All non-hydrogen atoms were refined anisotropically; hydrogen atoms were included into the model at their geometrically calculated positions and refined using a riding model. Disorder of one tetrahydrofuran solvate molecule was modeled over two sites with the use of free variables. Solvent disorder of a second solvate site consisting of 50:50 tetrahydrofuran:methanol was extensive and was treated as a diffuse contribution to the overall scattering without specific atom positions by SQUEEZE/PLATON.

[Co₂(μ -Cl)₂Cl(CH₃OH)(DPFN)]₂[CoCl₄]₃·3.75CH₃OH·0.5THF (**2**). All non-hydrogen atoms were refined anisotropically except for a CoCl₄²⁻ chloride atom and the atoms of a methanol molecule that had very low structural occupancy factors; hydrogen atoms were included into the model at their geometrically calculated positions and refined using a riding

model except the OH hydrogen atoms of the coordinated methanol ligands which were located from the electron difference map and the OH bond lengths were restrained to chemically appropriate values. Disorder of the CoCl_4^{2-} was modeled as partial occupancies over three sites. Methanol and the diethyl ether solvate molecules were modeled with partial occupancies appropriate to the electron density. Due to disorder of the diethyl ether solvate molecule bond and angle restraints at chemically appropriate values were applied and isotropic restraints were applied to atoms with severe anisotropy.

$[\text{Ni}_2(\mu\text{-Cl})_2\text{Cl}(\text{CH}_3\text{OH})(\text{DPFN})][\text{Cl}]\cdot 3.25\text{CH}_3\text{OH}$ (**4**). All non-hydrogen atoms were refined anisotropically; hydrogen atoms were included into the model at their geometrically calculated positions and refined using a riding model except the OH hydrogen atom of one coordinated methanol ligand which was located from the electron difference map and the OH bond length restrained to a chemically appropriate value. Significant disorder in the other coordinated methanol ligand prevented location of the OH hydrogen atom and the carbon atom was treated with a tight isotropic restraint. One chloride anion was disordered and modeled over two sites with the use of free variables. Extensive disorder of the methanol solvate molecules consisting of 13 methanol molecules could not be refined and was treated as a diffuse contribution to the overall scattering without specific atom positions by SQUEEZE/PLATON.

$[\text{Cu}_4(\mu\text{-Cl})_6(\text{DPFN})_2][\text{Cl}]_2\cdot 2\text{CH}_3\text{OH}\cdot 2\text{THF}$ (**5**). All non-hydrogen atoms were refined anisotropically; hydrogen atoms were included into the model at their geometrically calculated positions and refined using a riding model. The methanol solvate molecule sites were modeled as partially occupied and treated with isotropic restraints. The tetrahydrofuran molecule site was centered on a two-fold axis and one atom site was modeled as a 50:50 mixture of oxygen and carbon.

$[\text{Cu}_2(\mu\text{-OH})_2(\text{NO}_3)(\text{OH}_2)(\text{DPFN})]\cdot 2\text{H}_2\text{O}$ (**6**). All non-hydrogen atoms were refined anisotropically; hydrogen atoms were included into the model at their geometrically calculated positions and refined using a riding model except for hydrogen atoms of solvate water molecules and coordinated aquo or hydroxo ligands that were located from the electron difference map.

Acknowledgements

Support for T.C.D. was provided by a National Science Foundation Graduate Research Fellowship and a University of California Chancellor's Fellowship. This work was supported by the Director, Office of Energy Research, Office of Basic Energy Sciences, Chemical Sciences Division, of the U.S. Department of Energy under contract DE-AC02-05CH11231.

Notes and references

^a Department of Chemistry, University of California, Berkeley

Berkeley, CA 94720-1460, USA and Chemical Sciences Division, Lawrence Berkeley National Laboratory, Berkeley, CA 94720, USA.

E-mail: tdtalley@berkeley.edu

Electronic Supplementary Information (ESI) available: CIF files. See DOI: 10.1039/b000000x/

1. A. L. Gavrilova and B. Bosnich, *Chem. Rev.*, 2004, **104**, 349–384.
2. N. H. Williams, B. Takasaki, M. Wall and J. Chin, *Acc. Chem. Res.*, 1999, **32**, 485–493.
3. E. K. van den Beuken and B. L. Feringa, *Tetrahedron*, 1998, **54**, 12985–13011.
4. R. E. Stenkamp, *Chem. Rev.*, 1994, **94**, 715–726.
5. A. C. Rosenzweig, C. A. Frederick, S. J. Lippard and P. Nordlund, *Nature*, 1993, **366**, 537–543.
6. P. Nordlund, B.-M. Sjöberg and H. Eklund, *Nature*, 1990, **345**, 593–598.
7. E. Jabri, M. B. Carr, R. P. Hausinger and P. A. Karplus, *Science*, 1995, **268**, 998–1004.
8. N. Strater, T. Klabunde, P. Tucker, H. Witzel and B. Krebs, *Science*, 1995, **268**, 1489–1492.
9. C. Gerdemann, C. Eicken and B. Krebs, *Acc. Chem. Res.*, 2002, **35**, 183–191.
10. Z. F. Kanyo, L. R. Scolnick, D. E. Ash and D. W. Christianson, *Nature*, 1996, **383**, 554–557.
11. P. E. M. Siegbahn, *Acc. Chem. Res.*, 2009, **42**, 1871–1880.
12. J. A. Gilbert, D. S. Eggleston, W. R. Murphy, D. A. Geselowitz, S. W. Gersten, D. J. Hodgson and T. J. Meyer, *J. Am. Chem. Soc.*, 1985, **107**, 3855–3864.
13. S. W. Gersten, G. J. Samuels and T. J. Meyer, *J. Am. Chem. Soc.*, 1982, **104**, 4029–4030.
14. F. Liu, J. J. Concepcion, J. W. Jurss, T. Cardolaccia, J. L. Templeton and T. J. Meyer, *Inorg. Chem.*, 2008, **47**, 1727–1752.
15. Z. Deng, H.-W. Tseng, R. Zong, D. Wang and R. Thummel, *Inorg. Chem.*, 2008, **47**, 1835–1848.
16. H. Isobe, K. Tanaka, J.-R. Shen and K. Yamaguchi, *Inorg. Chem.*, 2014, **53**, 3973–3984.
17. H. Steinhagen and G. Helmchen, *Angew. Chem. Int. Ed.*, 1996, **35**, 2339–2342.
18. C. J. McKenzie and R. Robson, *J. Chem. Soc. Chem. Commun.*, 1988, 112–114.
19. I. Gamba, S. Palavicini, E. Monzani and L. Casella, *Chem. – Eur. J.*, 2009, **15**, 12932–12936.
20. I. Siewert, C. Limberg, S. Demeshko and E. Hoppe, *Chem. – Eur. J.*, 2008, **14**, 9377–9388.
21. J. Klingele, S. Dechert and F. Meyer, *Coord. Chem. Rev.*, 2009, **253**, 2698–2741.
22. P. J. Steel, *Coord. Chem. Rev.*, 1990, **106**, 227–265.
23. B. Bosnich, *Inorg. Chem.*, 1999, **38**, 2554–2562.
24. C. He and S. J. Lippard, *Tetrahedron*, 2000, **56**, 8245–8252.
25. C. He and S. J. Lippard, *Inorg. Chem.*, 2000, **39**, 5225–5231.
26. C. He, A. M. Barrios, D. Lee, J. Kuzelka, R. M. Davydov and S. J. Lippard, *J. Am. Chem. Soc.*, 2000, **122**, 12683–12690.
27. C. He, J. L. DuBois, B. Hedman, K. O. Hodgson and S. J. Lippard, *Angew. Chem. Int. Ed.*, 2001, **40**, 1484–1487.
28. T. C. Davenport and T. D. Tilley, *Angew. Chem. Int. Ed.*, 2011, **50**, 12205–12208.
29. G. K.-Y. Ng, J. W. Ziller and A. S. Borovik, *Chem. Commun.*, 2012, **48**, 2546–2548.
30. O. R. Evans, A. T. Bell and T. D. Tilley, *J. Catal.*, 2004, **226**, 292–300.
31. E. Hoppe, C. Limberg and B. Ziemer, *Inorg. Chem.*, 2006, **45**, 8308–8317.
32. T. C. Davenport, H. S. Ahn, M. S. Ziegler and T. D. Tilley, *Chem. Commun.*, 2014, **50**, 6326–6329.
33. D. F. Evans, *J. Chem. Soc.*, 1959, 2003–2005.
34. B. N. Figgis and J. Lewis, in *Progress in Inorganic Chemistry*, ed. F. A. Cotton, John Wiley & Sons, Inc., 2007, pp. 37–239.

35. N. S. Gill and R. S. Nyholm, *J. Chem. Soc.*, 1959, 3997–4007.
36. A. B. P. Lever, *Inorganic Electronic Spectroscopy*, Elsevier, New York, 2nd edn., 1984.
37. L. Meites and P. Zuman, *CRC Handbook Series in Organic Electrochemistry*, CRC Press, 1977, vol. 1.
38. J. Springborg, in *Advances in Inorganic Chemistry*, ed. A.G. Sykes, Academic Press, 1988, vol. 32, pp. 55–169.
39. R. J. M. Klein Gebbink, R. T. Jonas, C. R. Goldsmith and T. D. P. Stack, *Inorg. Chem.*, 2002, **41**, 4633–4641.
40. A. M. Barrios and S. J. Lippard, *Inorg. Chem.*, 2001, **40**, 1060–1064.
41. S. Roggan, C. Limberg, C. Knispel and T. D. Tilley, *Dalton Trans.*, 2011, **40**, 4315–4323.
42. H. Müller, B. Bauer-Siebenlist, E. Csapo, S. Dechert, E. Farkas and F. Meyer, *Inorg. Chem.*, 2008, **47**, 5278–5292.
43. E. Spodine, A. M. Atria, J. Manzur, A. M. García, M. T. Garland, A. Hocquet, E. Sanhueza, R. Baggio, O. Peña and J.-Y. Saillard, *J. Chem. Soc. Dalton Trans.*, 1997, 3683–3690.